

The 3–D X-ray Ejecta Structure of Tycho’s Supernova Remnant

MATTHEW J. MILLARD,¹ SANGWOOK PARK,¹ TOSHIKI SATO,² JOHN P. HUGHES,³ PATRICK SLANE,⁴ DANIEL PATNAUDE,⁵
DAVID BURROWS,⁶ AND CARLES BADENES⁷

¹*Box 19059, Department of Physics, University of Texas at Arlington, Arlington, TX 76019*

²*Department of Physics, Rikkyo University, 3-34-1 Nishi Ikebukuro, Toshima-ku, Tokyo 171-8501, Japan*

³*Department of Physics and Astronomy, Rutgers University, 136 Frelinghuysen Road, Piscataway, NJ 08854-8019, USA*

⁴*Harvard-Smithsonian Center for Astrophysics, 60 Garden Street, Cambridge, MA 02138, USA*

⁵*Smithsonian Astrophysical Observatory, Cambridge, MA 02138, USA*

⁶*Dept. of Astronomy & Astrophysics, Penn State University, University Park, PA 16802 USA*

⁷*Department of Physics and Astronomy and Pittsburgh Particle Physics, Astrophysics and Cosmology Center (PITT PACC), University of Pittsburgh, 3941 O’Hara Street, Pittsburgh, PA 15260, USA*

ABSTRACT

We present our velocity measurements of 59 clumpy, metal-rich ejecta knots in the supernova remnant (SNR) of SN 1572 (Tycho). We use our 450 ks Chandra High Energy Transmission Grating Spectrometer observation to measure the Doppler shift of the He-like Si K α line-center wavelength emitted from these knots to find their line-of-sight (radial) velocities (v_r). We find v_r up to ~ 5500 km s⁻¹, with roughly consistent speeds between blueshifted and redshifted ejecta knots. We also measure the proper motions (PMs) for our sample based on archival Chandra Advanced CCD Imaging Spectrometer data taken from 2003, 2009, and 2015. We estimate PMs up to $0''35$ yr⁻¹, which corresponds to a transverse velocity of about 5800 km s⁻¹ for the distance of 3.5 kpc to Tycho. Our v_r and transverse velocity measurements imply space velocities of $\sim 1900 - 6000$ km s⁻¹ for the ejecta knots in Tycho. We estimate a new expansion center of R.A.(J2000) = $00^{\text{h}}25^{\text{m}}18^{\text{s}}.725 \pm 1^{\text{s}}.157$ and decl.(J2000) = $+64^{\circ}08'02''.5 \pm 11''.2$ from our PM measurements, consistent to within $\sim 13''$ of the geometric center. The distribution of space velocities throughout the remnant suggests that the southeast quadrant generally expands faster than the rest of the SNR. We find that blueshifted knots are projected more in the northern shell, while redshifted knots are more in the southern shell. The previously estimated reverse shock position is consistent with most of our estimated ejecta distribution, however some ejecta show deviations from the 1-D picture of the reverse shock.

1. INTRODUCTION

Type Ia supernovae (SNe) are unique among the various types of SNe because they result from a similar physical process, the thermonuclear explosion of a white dwarf that has acquired enough mass to approach the Chandrasekhar limit ($\sim 1.4 M_{\odot}$) through either a merger with or mass transfer from a binary companion. Thus, the population of Type Ia SNe are more homogeneous than core-collapse SNe types, which have a wide range of progenitor masses. However, the intrinsic luminosities and colors of Type Ia SNe still vary (Jha et al. 2006; Maeda et al. 2011). Asymmetries in the explosion may contribute to their observed differences. In these cases, the viewing angle may be the cause of peculiar features observed from some SNe but not from others (Maeda et al. 2011). A direct method for investigating the explosion asymmetry of an SN is to measure the distribution of the ejecta in the resulting supernova remnant (SNR). The ejecta in SNRs that are only a few hundred years old have yet to be significantly disturbed by interactions with the surrounding interstellar medium (ISM). Thus, the explosion details of the SN may be preserved in the ejecta distribution. Since SNe are inherently 3–D events, the structure of an SNR should ultimately be studied in 3–D.

Tycho’s SNR (Tycho, hereafter) is the remnant of the Galactic historical supernova SN 1572. Due to its young age, its well-documented SN light curve and its close proximity to Earth ($\sim 2 - 4$ kpc, see Hayato et al. (2010)), Tycho is an ideal choice for studying the structure of a Type Ia SNR (e.g., Warren et al. (2005)). Both the X-ray spectrum of the SNR (Badenes et al. 2006) and the optical spectrum of the light echo (Krause et al. 2008b) indicate that Tycho is the remnant of a normal Type Ia supernova, neither subluminous nor overluminous. Tycho appears generally circular in shape, with a diameter of $\sim 8'$ in radio and X-ray wavelengths. XMM-Newton observations of Tycho showed an

overall uniform distribution of X-ray emitting knots and filaments of shocked ejecta gas (Decourchelle et al. 2001). The X-ray spectrum shows bright emission from the shocked metal-rich ejecta, indicating that Si, S, Ar, Ca, and Fe abundances are several times greater than solar values (Hwang et al. 1998). Suzaku data showed Doppler broadening of X-ray emission lines over large areas of the SNR that suggest a generally spherical expanding ejecta shell (Hayato et al. 2010). Williams et al. (2017) measured the speeds of blueshifted and redshifted ejecta knots with the Chandra Advanced CCD Imaging Spectrometer (ACIS) data and found no clear evidence for significant asymmetry in the ejecta distribution in Tycho. In many respects, Tycho appears to be the remnant of a standard Type Ia SN explosion. In fact, Type Ia SNe in general show a low degree of continuum polarization, implying that large deviations from spherical symmetry are not common (Wang & Wheeler 2008).

Although Tycho may be regarded as the remnant of a close approximation of a standard Type Ia SN, it does contain aspherical features whose origin is not fully understood. A prominent example is in the southeast region of the SNR, where a group of metal-rich X-ray emitting ejecta clumps appears to have overtaken the forward shock (Vancura et al. 1995; Decourchelle et al. 2001; Wang & Chevalier 2001; Fang et al. 2018; Williams et al. 2020; Sato et al. 2020). These ejecta clumps protruding from the southeastern boundary of the SNR include Fe-rich ejecta gas that can be used to pinpoint specific nucleosynthesis models, e.g., an incomplete Si burning or an α -rich freeze-out regime (Yamaguchi et al. 2017). This is in contrast to the western side of the remnant, where there is obvious separation between the ejecta and forward shock (Warren et al. 2005). A Chandra study of the proper motions of reverse-shocked gas showed large azimuthal variations on the order of 50%, while a Spitzer study suggested an ambient density enhancement by a factor of $\sim 3 - 10$ in the northeastern regions compared to the southwest portion of the remnant (Williams et al. 2013). Sato et al. (2019) hydrodynamically simulated Tycho’s clumpy structure assuming initially clumped ejecta, as well as perfectly smooth ejecta, in all cases evolving through a uniform ambient medium. Even for the perfectly smooth case, a clumpy structure appears in the ejecta due to Rayleigh–Taylor and Kelvin–Helmholtz instabilities. However, the observed structure in Tycho is more consistent with an initial clumped ejecta structure from the SN rather than instabilities arising from the ejecta interaction with the ambient medium. The optical light echo spectrum of Tycho shows an uncommon high-velocity Ca II absorption feature (Krause et al. 2008a), and thus an asymmetry in the ejecta distribution may have developed early in the evolution of the SNR, or in the SN itself. Sato & Hughes (2017a) performed detailed spectral fits on 27 individual X-ray emitting ejecta clumps across Tycho. They found a disparity in the maximum velocities of redshifted and blueshifted features, $\lesssim 7800 \text{ km s}^{-1}$ and $\lesssim 5000 \text{ km s}^{-1}$, respectively. The authors also noted large-scale He-like Si K α line centroid shifts across the SNR, on the order of arcminutes. They suggested that the apparent shifts may be due to differences in the intrinsic intensity of the approaching and receding sides of Tycho.

Here, we investigate the line-of-sight velocity distributions of the clumpy metal-rich ejecta in Tycho based on our deep 450 ks Chandra High Energy Transmission Grating (HETG) observation. The high resolution HETG spectroscopy has significant advantages over the ACIS spectroscopy in several aspects. For example, the gain energies of the ACIS detectors vary by up to 0.3% of the laboratory values¹. For the He-like Si K α energy, this corresponds to an estimated uncertainty in the line-of-sight (radial) velocity up to 900 km s^{-1} . The type of CCD array, either ACIS-I or ACIS-S, also adds uncertainties to the line-center energies (Sato & Hughes 2017a). ACIS data show considerable systematic uncertainties on the emission line-center energy depending on background subtraction regions. These effects contribute to overall systematic uncertainties of up to 2000 km s^{-1} in ACIS radial velocity (v_r) measurements (Sato & Hughes 2017a). The dispersed HETG spectroscopy can avoid such systematic uncertainties associated with the ACIS spectroscopy. Absolute wavelength uncertainties in line-center measurements with the HETG are generally $\lesssim 100 \text{ km s}^{-1}$ (Marshall et al. 2004; Ishibashi et al. 2006)². Thus, HETG line-center energy measurements are dominated by statistical uncertainties, while the ACIS line-center measurements are dominated by systematic uncertainties. In this work, we combine our radial velocity measurements of clumpy ejecta knots using our deep HETG data with the proper motion measurements of those knots using archival ACIS imaging data-sets to build a 3-D picture of the overall ejecta structure. In Section 2, we present the details of our deep Chandra HETG observation. In Section 3, we report our analysis and results, and in Section 4 we discuss our interpretations. We conclude our study in Section 5.

¹ https://cxc.harvard.edu/proposer/POG/html/chap6.html#tth_sEc6.8

² <https://cxc.harvard.edu/proposer/POG/html/chap8.html>

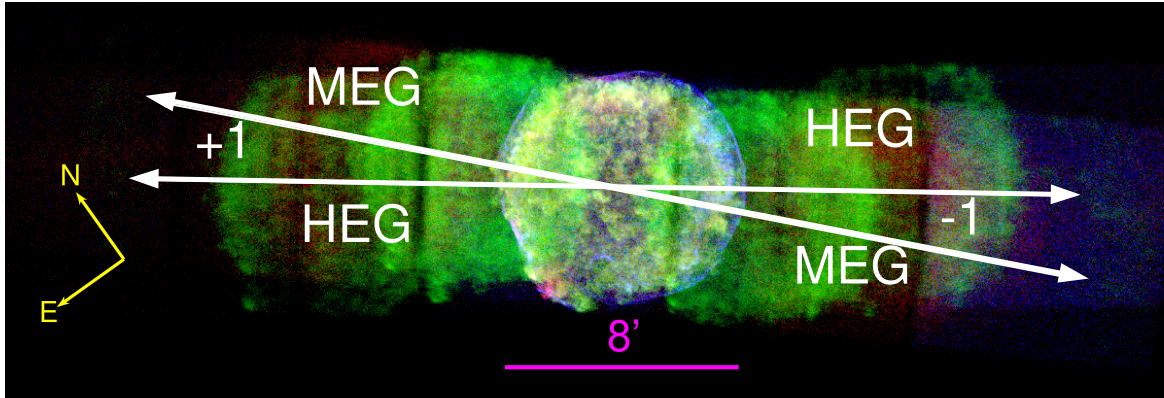


Figure 1. Chandra HETG 3-color dispersed image of Tycho. Red: 0.7-1.2 keV, Green: 1.7-2.0 keV and Blue: 4.0-8.0 keV. Our color codes are selected to represent the Fe L line complex (red), He-like Si $K\alpha$ lines (green), and the continuum-dominated band (blue), respectively. The white arrows show the dispersion directions of the Medium and High Energy Gratings.

2. OBSERVATIONS

We performed our Chandra HETG observations of Tycho from 2017 October 17 to 2017 November 19. The aimpoint was set at R.A. (J2000) = $00^{\text{h}}25^{\text{m}}19^{\text{s}}.0$, decl. (J2000) = $+64^{\circ}08'10''.0$, which is close to the geometric center of the roughly circular SNR. The date and exposure time of each observation are listed in Table 1. The total effective exposure time is 443 ks. We processed the raw event files using Chandra Interactive Analysis of Observations (CIAO) (Fruscione et al. 2006) version 4.11 and the Chandra Calibration Database (CALDB) version 4.8.2 to create a new level=2 event file using the CIAO command, `chandra_repro`. We extracted the 1st-order dispersed spectra from a number of small regions across the SNR (Section 3.3) using the TGCat scripts (Huenemoerder et al. 2011) `tg_create_mask`³, `tg_resolve_events`⁴, and `tgextract`⁵, and created the full set of corresponding detector response files using the script, `make_responses`, which accounts for the zeroth-order position and dispersed region size and orientation. The HETG-dispersed image of Tycho is shown in Figure 1.

We also use archival ACIS-I observations of Tycho (Table 2) to supplement the HETG data analysis. For the ObsIDs taken in 2009, we combined all 9 individual ObsIDs, re-projecting them onto ObsID 10095 which had the longest exposure. The main purpose of our archival ACIS data analysis is to measure proper motions of small ejecta knots in Tycho. Thus, we re-align these ACIS images taken at three different epochs using the `reproject_aspect` command in CIAO, accounting for the astrometric correction based on 5 to 16 background point sources (depending on the ObsID) with their sky positions identified in the NASA/IPAC Extragalactic Database (NED)⁶.

3. DATA ANALYSIS AND RESULTS

3.1. Region Selection

Based on the archival Chandra ACIS observation of Tycho, we identified clumpy emission features that are bright in the Si $K\alpha$ (1.7 - 2.0 keV) band as candidate targets for HETG spectral extraction. We extracted their individual 1st-order Medium Energy Grating (MEG) spectra from our Chandra HETG observation. In Figure 1, it is clear that the zeroth-order and 1st-order images overlap. In some regions, this overlap may cause the 1st-order HETG spectrum to be contaminated by the overlapping zeroth-order emission. To avoid these regions, we compared the counts in the +1 and -1 order spectra. The majority of the knots in our sample have a +1 to -1 order counts ratio that is within a factor of ~ 2 . This difference in counts is consistent with the variations in effective area across the +1 and -1 order legs in the Si $K\alpha$ band⁷, and thus their dispersed spectra are unlikely to be significantly affected by the zeroth order emission. We note that two knots in our sample (SW3 and SW7) have a larger disparity in counts between the +1 and -1 orders, up to a factor of 5. The v_r estimates for these knots may be less reliable due to possible contamination

³ http://cxc.harvard.edu/ciao/ahelp/tg_create_mask.html

⁴ http://cxc.harvard.edu/ciao/ahelp/tg_resolve_events.html

⁵ http://cxc.harvard.edu/ciao/ahelp/tg_extract.html

⁶ <https://ned.ipac.caltech.edu/>

⁷ See footnote 2

from the zeroth order emission. Applying similar methods to those developed by Millard et al. (2020), we select 59 small candidate ejecta regions (angular sizes of $\sim 3'' - 10''$) to measure the He-like Si $K\alpha$ line-center energy (~ 1.86 keV) for each region. We selected target regions such that similarly bright emission features are at least $\sim 20''$ away along the dispersion direction to avoid spectral contamination. We generally avoided choosing knots for our sample that are asymmetrically extended in the dispersion direction. Each region has at least 200 1st order MEG counts in the Si $K\alpha$ band.

Table 1. Chandra HETG Observations of Tycho’s SNR

Observation ID	Start Date	Exposure Time (ks)
19293	2017-10-17	49.7
20813	2017-10-21	47.8
20822	2017-10-23	13.9
19292	2017-10-26	19.8
20820	2017-10-27	30.5
20819	2017-10-29	44.5
19291	2017-10-30	40.0
20832	2017-11-01	50.1
20833	2017-11-03	34.6
20834	2017-11-04	35.9
20835	2017-11-06	27.6
20799	2017-11-17	22.2
20821	2017-11-19	25.6

Table 2. Archival Chandra ACIS-I Observations of Tycho’s SNR

Observation ID	Start Date	Exposure Time (ks)
3837	2003-04-29	144.6
10093	2009-04-13	117.6
10094	2009-04-18	89.9
10095	2009-04-23	173.4
10096	2009-04-27	104.9
10097	2009-04-11	106.9
10902	2009-04-15	39.3
10903	2009-04-17	23.9
10904	2009-04-13	34.7
10906	2009-05-03	40.9
15998	2015-04-22	146.7

3.2. Ejecta Identification

To identify the overabundant nature of the ejecta-dominated regions (out of our 59 selected candidate regions), we performed spectral model fits for each individual regional spectrum based on the combined 2009 archival Chandra ACIS data (merging all ObsIDs taken in 2009, to achieve the total of ~ 731 ks). We fitted the observed 1.6 – 4.5 keV band ACIS spectrum extracted from each region with an absorbed `vpshock` model (Borkowski et al. 2001) using the XSPEC software package version 12.10.1 (Arnaud 1996). We estimated the background spectrum using an annulus region encircling the entire remnant. Then, we subtracted the background spectrum from the regional source spectra before fitting them with the spectral model. We fixed the absorption column at $N_H = 8 \times 10^{21} \text{ cm}^{-2}$ for Tycho (Foight et al. 2016). We allowed the electron temperature, kT , and ionization timescale, τ ($\tau = n_e t$, where n_e is the electron density, and t is the time since being shocked), to vary. We also varied the redshift, normalization, and abundances of Si, S, Ar, and Ca. Since contributions from other elements are negligible in the 1.6 – 4.5 keV band, we fixed all other elemental abundances at solar values (Wilms et al. 2000). The model gave satisfactory fits to the data, with reduced chi-squared values ranging from $\chi^2/dof = 51/73 - 119/60$. We confirm that the best-fit abundances are several times solar values, indicating that all knots in our sample are ejecta-dominated. The best-fit electron temperatures of the ejecta knots in our sample are $kT_e \sim 1 - 5 \text{ keV}$, with ionization timescales $\tau \sim 2 - 50 \times 10^{10} \text{ cm}^{-3} \text{ s}$, generally consistent with the typical ejecta values reported in Williams et al. (2017).

3.3. Radial Velocities of Ejecta

To measure the radial velocity of each X-ray emission feature in our sample, we adopt the method used in Millard et al. (2020), using the Interactive Spectral Interpretation System (ISIS) software package version 1.6.2 (Houck & Denicola 2000). The spatially integrated broadband ACIS spectrum of Tycho shows bright Si, S, Ar, Ca, and Fe emission lines. However, we are interested in the HETG spectra of small features that are only a few arcseconds across. The small region sizes and the low HETG detection efficiency greatly reduces the prominence of most of these lines. Ultimately, our HETG spectra of these small emission features are dominated by the He-like Si-K α line. For each of our regional spectra, we measure the line-center energies in the Si K α band by fitting six Gaussian curves to the spectrum to account for the three He-like Si K α lines (6.648 Å for resonance, 6.688 Å for intercombination, 6.740 Å for the forbidden line), and two Li-like Si XII lines at 6.717 Å and 6.782 Å (Drake 1988) and one for the diffuse background emission of the SNR. We jointly fit the model to the MEG +/- 1 order spectra, tying the line-center wavelengths between spectra dispersed along the positive and negative arms. To account for the extent of the emission along the dispersion direction, the widths of the Gaussian curves are allowed to vary. The widths of the five source Gaussians are tied, while the width of the background Gaussian component varies independently and is generally much broader. Since the individual spectral lines may not be clearly resolved due to the extended nature of the ejecta knots, we fix the flux ratios among the triplet He-like Si K α lines and Li-like Si lines at those corresponding to the best-fit electron temperature and ionization timescale for each region (Section 3.2). We compared our measured line-center wavelength with the rest value for the resonance line at 6.648 Å, which is generally the strongest among the five lines in our model. The difference between the rest and observed values gives the Doppler shift, which we use to estimate the v_r for each knot. The location of each knot is marked in Figure 2a, and our results are summarized in Table 3. Example HETG spectra and best-fit models for the +1 and -1 arms are shown in Figures 2b and 2c.

In Figure 2a, we show regions for which we measure Doppler shifts of Si lines. Our measured v_r ranges from ~ -5200 to $+5300 \text{ km s}^{-1}$. We note that our sample partially overlaps with those studied by Sato & Hughes (2017a) and Williams et al. (2017) (SH17a and W17, hereafter), who measured the v_r of small ejecta regions in Tycho based on the lower-resolution ACIS spectroscopy: i.e., 15 and 19 regions of our sample are also included in SH17a and W17, respectively. We find general agreement between our measured values and those from ACIS data, as shown in Figure 3. We found a few exceptions where our measured radial velocities are smaller than those in SH17a by a few 10^3 km s^{-1} (e.g., regions C6 and SW3). The origin of the discrepancy is unclear, but may be due in part to confusion from neighboring emission. Contributions from the diffuse expanding hemispheres of the remnant may be present even in small extraction regions of only a few arcseconds in diameter, and could influence the ACIS velocity estimates.

It is remarkable that we measure a highly significant radial velocity of $v_r = -1860 \pm 170 \text{ km s}^{-1}$ for the SE protrusion (region SE3 in Figure 2a). This v_r has been suggested based on the ACIS spectroscopy, but was not constrained due to large uncertainties of a few 10^3 km s^{-1} (SH17a; W17). Based on our high resolution HETG spectroscopy, we accurately measure (within $\sim 10\%$ uncertainties) this intriguing v_r for an ejecta feature projected beyond the main shell of the SNR with an order of magnitude improved accuracy.

Table 3. Radial Velocity and Proper Motion Measurements of Ejecta Features in Tycho's SNR

Region	R.A. ^a	Decl. ^a	D^b	v_r	μ_{RA}^c	μ_{Dec}^c	μ_{Tot}^d	η^e	v_s^f
	(degree)	(degree)	(arcmin)	(km s ⁻¹)	(arcsec yr ⁻¹)	(arcsec yr ⁻¹)	(arcsec yr ⁻¹)		(km s ⁻¹)
SE1	6.48336	64.130282	4.07	-2470 ⁺⁴¹⁰ ₋₄₂₀	-0.323 ± 0.064	-0.002 [*]	0.323 ± 0.064	0.6 ± 0.12	5910 ± 980
SE2	6.47022	64.128169	3.74	-670 ± 560	-0.09 ± 0.064	-0.057 ± 0.04	0.106 ± 0.066	0.21 ± 0.13	1890 ± 1040
SE3	6.49035	64.125542	4.28	-1860 ± 170	-0.299 ± 0.063	-0.096 ± 0.04	0.314 ± 0.064	0.56 ± 0.11	5530 ± 1000
SE4	6.46192	64.12032	3.6	1650 ⁺⁶⁹⁰ ₋₇₁₀	-	-	-	-	-
SE5	6.40962	64.125008	2.2	3840 ± 820	-	-	-	-	-
SE6	6.47617	64.106979	4.21	1660 ± 660	-0.249 ± 0.062	-0.061 ± 0.038	0.257 ± 0.063	0.45 ± 0.11	4580 ± 1000
SE7	6.46718	64.10879	3.95	1380 ⁺⁶¹⁰ ₋₆₂₀	-0.314 ± 0.063	0.06 ± 0.035	0.32 ± 0.063	0.6 ± 0.12	5490 ± 1020
SE8	6.41552	64.118707	2.47	2780 ⁺⁶⁹⁰ ₋₇₁₀	-0.238 ± 0.061	-0.086 ± 0.033	0.253 ± 0.061	0.76 ± 0.18	5040 ± 930
SE9	6.3844	64.120199	1.69	4210 ⁺⁹⁸⁰ ₋₁₀₃₀	-	-	-	-	-
SE10	6.42579	64.099514	3.29	2780 ± 680	-	-	-	-	-
SE11	6.4111	64.088671	3.49	1070 ⁺⁷³⁰ ₋₇₄₀	-	-	-	-	-
SE12	6.36942	64.113216	1.65	-920 ± 490	-	-	-	-	-
SE13	6.39798	64.086552	3.39	2100 ± 430	-	-	-	-	-
SE14	6.36005	64.090842	2.72	5180 ⁺⁷⁷⁰ ₋₇₄₀	-0.012 [*]	-0.171 ± 0.04	0.172 ± 0.07	0.44 ± 0.19	5920 ⁺⁸⁸⁰ ₋₈₆₀
SE15	6.34372	64.085777	2.93	-20 [*]	-0.053 [*]	-0.326 ± 0.037	0.33 ± 0.067	0.8 ± 0.17	5480 ± 1110
NE1	6.36031	64.198296	3.95	960 ± 600	0.001 [*]	0.354 ± 0.038	0.354 ± 0.068	0.71 ± 0.13	5950 ± 1120
NE2	6.34541	64.162038	1.74	2460 ⁺¹⁰¹⁰ ₋₁₀₇₀	-0.001 [*]	0.158 ± 0.041	0.158 ± 0.071	0.77 ± 0.3	3600 ⁺¹¹⁰⁰ ₋₁₁₃₀
NE3	6.37907	64.182406	3.19	-2290 ⁺⁵⁹⁰ ₋₆₀₀	-0.029 [*]	0.243 ± 0.038	0.245 ± 0.068	0.61 ± 0.16	4670 ⁺¹⁰²⁰ ₋₁₀₃₀
NE4	6.35505	64.156519	1.52	-3590 ⁺⁴⁹⁰ ₋₅₀₀	-0.062 [*]	0.077 ± 0.038	0.099 ± 0.067	0.54 ± 0.33	3950 ⁺⁶⁴⁰ ₋₆₅₀
NE5	6.38373	64.178972	3.06	-4210 ⁺⁶⁰⁰ ₋₆₂₀	-	-	-	-	-
NE6	6.40231	64.193381	4.06	910 ⁺⁴⁶⁰ ₋₄₇₀	-0.125 ± 0.063	0.195 ± 0.038	0.231 ± 0.067	0.45 ± 0.12	3940 ± 1090
NE7	6.40808	64.189185	3.92	-400 [*]	-0.16 ± 0.063	0.207 ± 0.04	0.262 ± 0.068	0.53 ± 0.13	4360 ± 1130
NE8	6.40062	64.165145	2.66	-1800 ± 440 [*]	-0.126 ± 0.061	0.158 ± 0.034	0.202 ± 0.063	0.61 ± 0.18	3800 ⁺⁹⁵⁰ ₋₉₄₀
NE9	6.45171	64.179368	4.23	490 [*]	-0.133 ± 0.062	0.159 ± 0.035	0.207 ± 0.064	0.38 ± 0.11	3460 ± 1050
NE10	6.43524	64.161668	3.26	-1660 ⁺⁴⁹⁰ ₋₄₈₀	-0.204 ± 0.062	0.049 ± 0.035	0.21 ± 0.062	0.51 ± 0.14	3860 ± 950
NE11	6.46282	64.153989	3.72	100 [*]	-0.173 ± 0.062	0.021 [*]	0.174 ± 0.062	0.36 ± 0.12	2900 ± 1030
NW1	6.20057	64.139647	3.35	1900 ± 570	0.231 ± 0.064	-0.077 ± 0.038	0.244 ± 0.064	0.53 ± 0.14	4470 ± 990
NW2	6.1934	64.153122	3.7	-800 ± 670 [*]	0.264 ± 0.064	0.103 ± 0.039	0.284 ± 0.065	0.57 ± 0.13	4780 ± 1070
NW3	6.22578	64.149849	2.84	-310 [*]	0.17 ± 0.064	0.071 ± 0.036	0.185 ± 0.064	0.48 ± 0.17	3080 ± 1060
NW4	6.21326	64.154398	3.24	1180 ± 580 [*]	0.227 ± 0.064	0.083 ± 0.038	0.242 ± 0.065	0.56 ± 0.15	4190 ± 1050
NW5	6.17947	64.160641	4.2	220 [*]	0.289 ± 0.065	0.155 ± 0.037	0.328 ± 0.066	0.6 ± 0.12	5450 ± 1100
NW6	6.25986	64.154143	2.15	-3980 ⁺⁶⁵⁰ ₋₆₆₀	0.162 ± 0.063	0.039 ± 0.037	0.167 ± 0.064	0.6 ± 0.22	4850 ⁺⁸¹⁰ ₋₈₂₀
NW7	6.25252	64.162735	2.62	-1000 ± 600	0.126 ± 0.064	0.14 ± 0.04	0.189 ± 0.068	0.55 ± 0.19	3290 ± 1090
NW8	6.26811	64.162003	2.3	-3430 ± 500	0.116 ± 0.063	0.081 ± 0.037	0.141 ± 0.065	0.47 ± 0.21	4150 ⁺⁷⁴⁰ ₋₇₃₀
NW9	6.29317	64.153676	1.49	5320 ⁺⁹²⁰ ₋₉₅₀	-	-	-	-	-
NW10	6.2808	64.16993	2.48	-2620 ⁺⁵⁶⁰ ₋₅₄₀	0.029 [*]	0.102 ± 0.034	0.106 ± 0.064	0.34 ± 0.19	3160 ⁺⁷⁵⁰ ₋₇₄₀
NW11	6.30679	64.162212	1.78	-1120 ± 640	-	-	-	-	-
NW12	6.30327	64.166397	2.05	-5220 ± 890	-	-	-	-	-
NW13	6.29901	64.192441	3.58	-80 [*]	-0.030 [*]	0.147 ± 0.04	0.15 ± 0.07	0.33 ± 0.14	2490 ± 1160
NW14	6.31804	64.168952	2.11	5280 ⁺⁹⁸⁰ ₋₂₀₇₀	0.031 [*]	0.149 ± 0.036	0.152 ± 0.065	0.58 ± 0.23	5860 ⁺¹⁰⁰⁰ ₋₁₉₂₀
SW1	6.28838	64.07014	3.97	160 [*]	-	-	-	-	-
SW2	6.29334	64.094728	2.53	1140 ± 520	0.076 ± 0.063	-0.194 ± 0.039	0.208 ± 0.068	0.57 ± 0.2	3640 ± 1080
SW3	6.30962	64.113309	1.33	3860 ⁺⁸⁷⁰ ₋₉₀₀	-	-	-	-	-
SW4	6.2801	64.091581	2.84	2060 ⁺⁵⁸⁰ ₋₅₆₀	0.061 [*]	-0.214 ± 0.036	0.223 ± 0.065	0.55 ± 0.17	4240 ± 980
SW5	6.27296	64.096338	2.68	840 ⁺⁴⁷⁰ ₋₄₈₀	0.111 ± 0.063	-0.106 ± 0.035	0.153 ± 0.064	0.4 ± 0.18	2680 ± 1020

Table 3 continued on next page

Table 3 (continued)

Region	R.A. ^a	Decl. ^a	D^b	v_r	μ_{RA}^c	μ_{Dec}^c	μ_{Tot}^d	η^e	v_s^f
	(degree)	(degree)	(arcmin)	(km s ⁻¹)	(arcsec yr ⁻¹)	(arcsec yr ⁻¹)	(arcsec yr ⁻¹)		(km s ⁻¹)
SW6	6.24856	64.084384	3.64	860_{-630}^{+680}	0.021 [*]	-0.208 ± 0.035	0.209 ± 0.065	0.41 ± 0.13	3570 ± 1060
SW7	6.28942	64.111983	1.67	$3010_{-580}^{+590 \dagger}$	-	-	-	-	-
SW8	6.25281	64.108776	2.49	2370_{-720}^{+730}	0.018 [*]	-0.073 ± 0.038	0.076 ± 0.067	0.21 ± 0.2	2680_{-820}^{+830}
SW9	6.22021	64.099009	3.52	2540 ± 700	0.153 ± 0.063	-0.068 ± 0.037	0.168 ± 0.064	0.34 ± 0.13	3760 ± 920
SW10	6.22228	64.105266	3.26	-1630 ± 340	0.21 ± 0.063	-0.154 ± 0.038	0.26 ± 0.065	0.57 ± 0.15	4620 ± 1020
SW11	6.27209	64.12145	1.65	2830_{-680}^{+700}	-	-	-	-	-
SW12	6.22676	64.120373	2.78	740_{-630}^{+640}	0.118 ± 0.063	-0.081 ± 0.036	0.143 ± 0.064	0.37 ± 0.17	2490 ± 1030
C1	6.3738	64.143253	1.32	-1700 ± 590	-	-	-	-	-
C2	6.36353	64.132469	0.93	-2860_{-570}^{+580}	-	-	-	-	-
C3	6.34361	64.139439	0.52	4460_{-770}^{+780}	-	-	-	-	-
C4	6.34296	64.130289	0.45	4060 ± 880	-	-	-	-	-
C5	6.33638	64.13981	0.41	3680_{-950}^{+870}	-	-	-	-	-
C6	6.31697	64.132757	0.3	3700_{-730}^{+850}	-	-	-	-	-
C7	6.31072	64.14762	0.93	4390_{-1210}^{+1040}	-	-	-	-	-

Errors represent a 90% confidence interval unless otherwise noted.

^a Position in 2015 (J2000).

^b Projected angular distance from our estimated kinematic center (see Section 4.3)

^c Includes systematic uncertainties (see Section 3.4).

^d $\mu_{Tot} = \sqrt{\mu_{R.A.}^2 + \mu_{decl.}^2}$.

^e Expansion index (see Section 3.4).

^f Estimated space velocity for a distance of 3.5 kpc.

^{*} The error interval includes 0, and thus the direction of motion is uncertain. We show only our best-fit value.

[†] This estimate may be affected due to spectral contamination from zeroth order emission (Section 3.1).

3.4. Ejecta Proper Motions

Based on the archival Chandra ACIS-I data from 2003, 2009, and 2015 (Table 2), we estimate the proper motions of the ejecta regions in our sample. To measure the proper motions, we apply the methods described in Sato et al. (2018). To find the position of each knot at different epochs, we took the image from the long observation in 2009 (ObsID 10095) as the reference image and compared it to the images from the 2003 and 2015 epochs filtered to the 1.6 – 4.5 keV band, which is dominated by the Si K α line. We incrementally shifted the 2003 and 2015 images in R.A. and decl. until a statistically good match with the reference image was obtained, i.e., the Cash statistic (Cash 1979) was minimized. To estimate the systematic uncertainties, we applied this image fitting method to five background point sources. We find the systematic uncertainties of our method to be $\sigma_{\mu_{RA}} = 0''.06 \text{ yr}^{-1}$ and $\sigma_{\mu_{decl.}} = 0''.03 \text{ yr}^{-1}$, in reasonable agreement with the uncertainties estimated in Katsuda et al. (2010). We were able to successfully measure proper motions for 37 of the 59 knots in our sample. For other knots, it was difficult to measure proper motions because they were faint or contaminated by complex emission features in the immediate surroundings. Regions projected close to the center of the SNR do not show measurable proper motions (as perhaps expected), and thus their space velocity is dominated by their radial velocity.

The results of our proper motion measurements are summarized in Table 3. Our measured values range from $-0''.32 \text{ yr}^{-1}$ to $+0''.29 \text{ yr}^{-1}$ in R.A. and $-0''.33 \text{ yr}^{-1}$ to $+0''.35 \text{ yr}^{-1}$ in decl. We define the expansion index, η , as $\mu_{Tot}/(D/t_{age})$, where t_{age} is the age of Tycho (445 years in this study), and D is the estimated angular distance from the geometric center. Our proper motion measurements suggest that all of the knots in the sample have undergone some significant

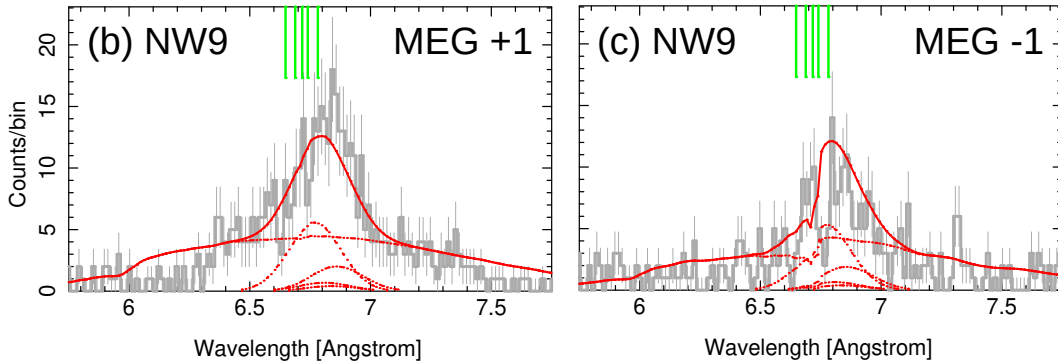
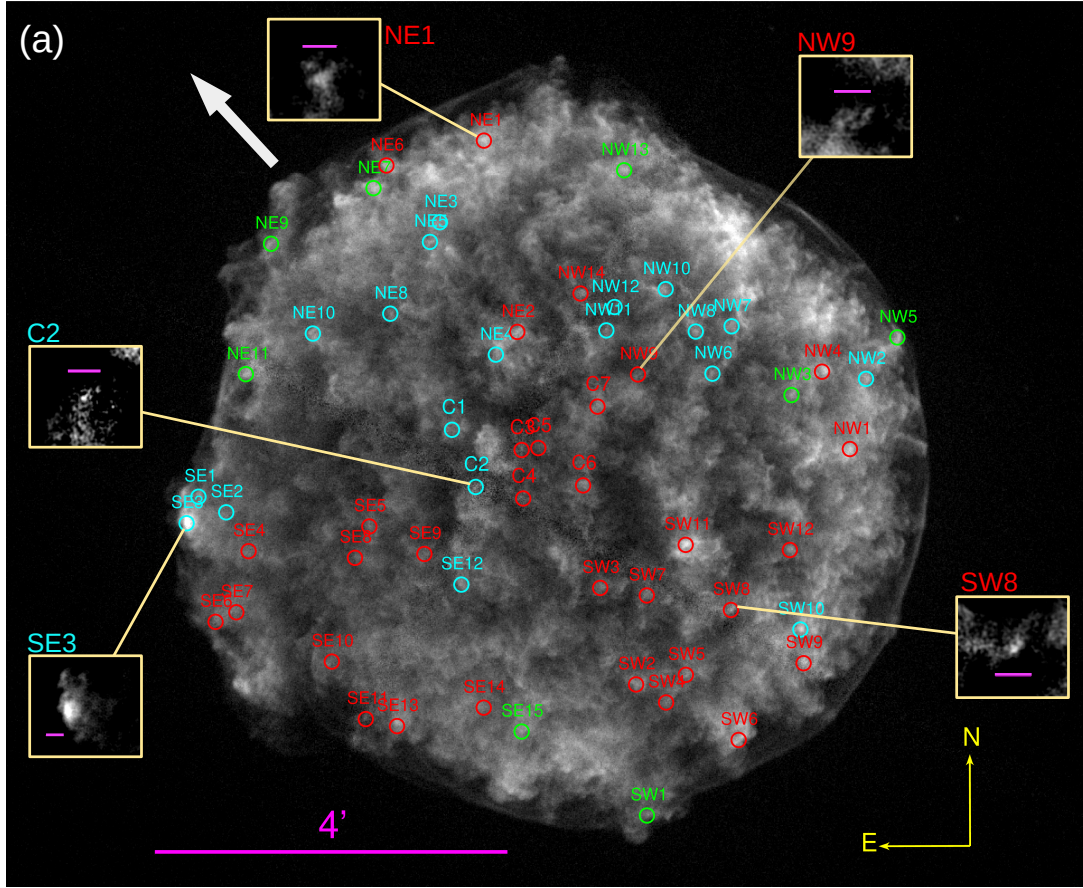


Figure 2. (a): An exposure-corrected Chandra ACIS image of Tycho’s SNR in the Si $K\alpha$ band (1.7 - 2.0 keV) based on the archival Chandra data taken in 2009. The fifty-nine ejecta knots analyzed in this work are marked with circles. The white arrow in the upper left indicates the dispersion direction. Cyan and red circles indicate blue- and red-shifted features, respectively, while green represents statistically negligible v_r at the 90% confidence interval. The image cutouts along the periphery show zoom-in views of example ejecta features. The scale bar in each cutout is $10''$ across. (b): An example of our line-center energy fit for region NW9. The MEG +1 spectrum is overlaid with our best-fit Gaussian model (Gray: data; Red: model fit). The dashed lines show individual Gaussian components of our best-fit model. The vertical green lines show the locations of the rest frame He-like Si $K\alpha$ and Li-like Si XII line-center wavelengths. (c): The same as (b), however the data and model are from the MEG -1 spectrum.

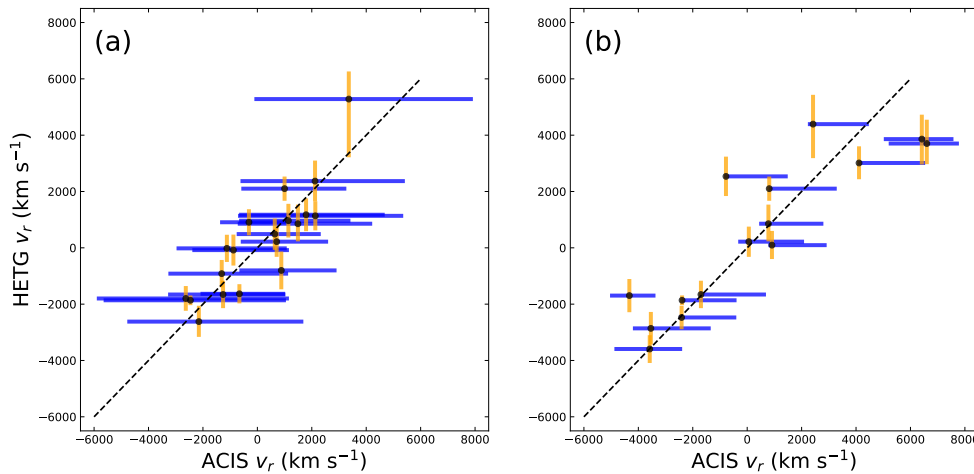


Figure 3. Comparison of Chandra HETG vs. ACIS measurements of radial velocity for the common samples of ejecta knots in Tycho between this work and (a) W17 and (b) SH17a. The error bars (blue) in the ACIS measurements include systematic uncertainties.

deceleration, ranging from $\eta = 0.21$ to 0.80 , with an average $\eta = 0.51$. The proper motion directions are shown in Figure 4.

We combine the radial velocity and proper motion measurements to estimate the 3-D space velocity of regions in our sample. We adopt a distance of 3.5 kpc to Tycho (Williams et al. 2013). At this distance, the transverse velocities of knots at the boundary and the radial velocities of knots projected near the center of the SNR generally agree, $v_r \sim 5500$ km s⁻¹, which is consistent with the maximum range of space velocities for ejecta regions in our sample. Combining the radial velocity and proper motions we estimate the space velocities of $\sim 1900 - 6000$ km s⁻¹, with an average $v_s \sim 4200$ km s⁻¹. These velocity ranges are in plausible agreement with those estimated by SH17a and W17, but with uncertainties smaller by a factor of ~ 3 on average.

4. DISCUSSION

4.1. Azimuthal Variations in Ejecta Velocity

In Figure 5, we plot our estimated space velocity for each knot against its azimuthal angle (position angles measured counter-clockwise from north). For knots projected closer to the center of the remnant, their true location along the periphery of the SNR is more uncertain. Thus, we only included knots with projected positions offset from the center where we have firmly estimated their proper motions. The ejecta knots in the southeast (SE) quadrant of Tycho have $v_s \sim 6000$ km s⁻¹, and thus appear to be among the fastest-moving knots ($\sim 40\%$ faster than the average space velocity of our sample). This high space velocity is in plausible agreement with the presence of ejecta bullet-like features (protrusions extending beyond the main SNR shell, (Wang & Chevalier 2001)) where high-speed overdense clumps overtake the forward shock. However, the protruding knots are not individual ejecta features like in Wang & Chevalier (2001), but are part of a large-scale portion of the ejecta that was propelled from the explosion more energetically than elsewhere in the remnant. The densities along the SE rim are larger by a factor of a few than those in the southwest (SW) (Williams et al. 2013). However, the ejecta space velocities in the SE are faster by a factor of ~ 2 than those in the SW. Thus, the ejecta velocities in SE regions may not be directly related to a rarefied ISM in that direction, but probably due to their intrinsically energetic nature. It is interesting to note that there is a prominent high-speed ejecta knot (NW5) approaching $v_{space} \sim 6000$ km s⁻¹ projected at the northwest (NW) boundary, in a nearly opposite direction from the protruding SE knots. While it is tempting to speculate strong ejecta outflows along the SE-NW axis connecting these particularly fast-moving knots, we find no additional substantial evidence to support such a bi-polar ejecta outflow along this axis.

In the northeast (NE), from position angles 10° to 100° , the ejecta space velocities appear to decrease, from ~ 6000 km s⁻¹ to ~ 2000 km s⁻¹. The space velocity then sharply rises back up to ~ 6000 km s⁻¹ for ejecta knots in the SE

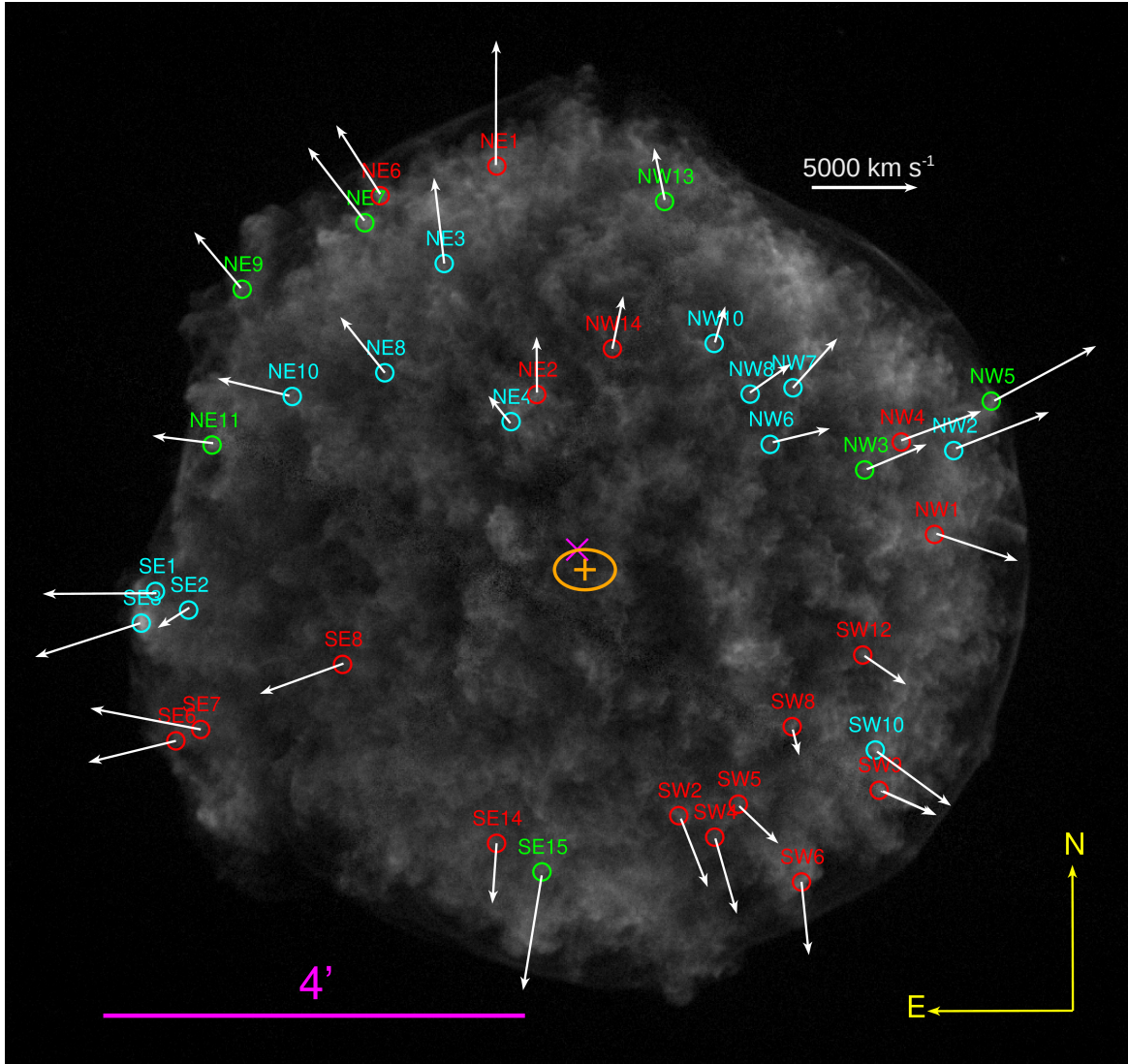


Figure 4. The subset of our regions where we measure the proper motion. Each white arrow shows the direction and relative magnitude of the proper motion for each knot. The length of the white arrow at the top right indicates a speed of 5000 km s^{-1} . The orange cross and ellipse indicate the position and uncertainty of our estimated kinematic center based on our proper motion measurements of ejecta knots (see Section 4.3). The magenta “X” indicates the geometric center (Warren et al. 2005). The image is the same as in Figure 2, scaled to make the arrows more visible.

from position angles $\sim 100^\circ - 170^\circ$, before decreasing again to $2000\text{--}4000 \text{ km s}^{-1}$ in the SW from 200° to 250° . Some decreases in ejecta velocity with azimuthal angle are coincident with increasing ambient density, suggesting an origin from the SNR’s interaction with a dense surrounding medium. A Spitzer study of the ratio of the 70 to $24 \mu\text{m}$ fluxes in Tycho revealed an increase of post-shock densities at the rim from azimuthal angles of roughly $10 - 80^\circ$ and $300 - 330^\circ$ (Williams et al. 2013), similar to the angle ranges of decreasing velocity (see Figure 5). The ejecta in these regions may have been slowed either by direct interaction with the higher-density ISM gas or by an enhanced reverse shock that developed due to the shock-ISM interaction, or a combination of both.

4.2. 3-D Ejecta Structure

The X-ray emitting knots and filaments of the shocked ejecta gas in Tycho are distributed, in general, uniformly across the face of the SNR (Figures 2 and 6a). Our kinematic study of these ejecta knots shows that the overall spatial and velocity distributions of ejecta in Tycho are relatively smooth, in contrast to the case of Kepler’s SNR where significant deviations from a spherical distribution, such as the “Ears” and nearly freely-expanding ejecta knots are

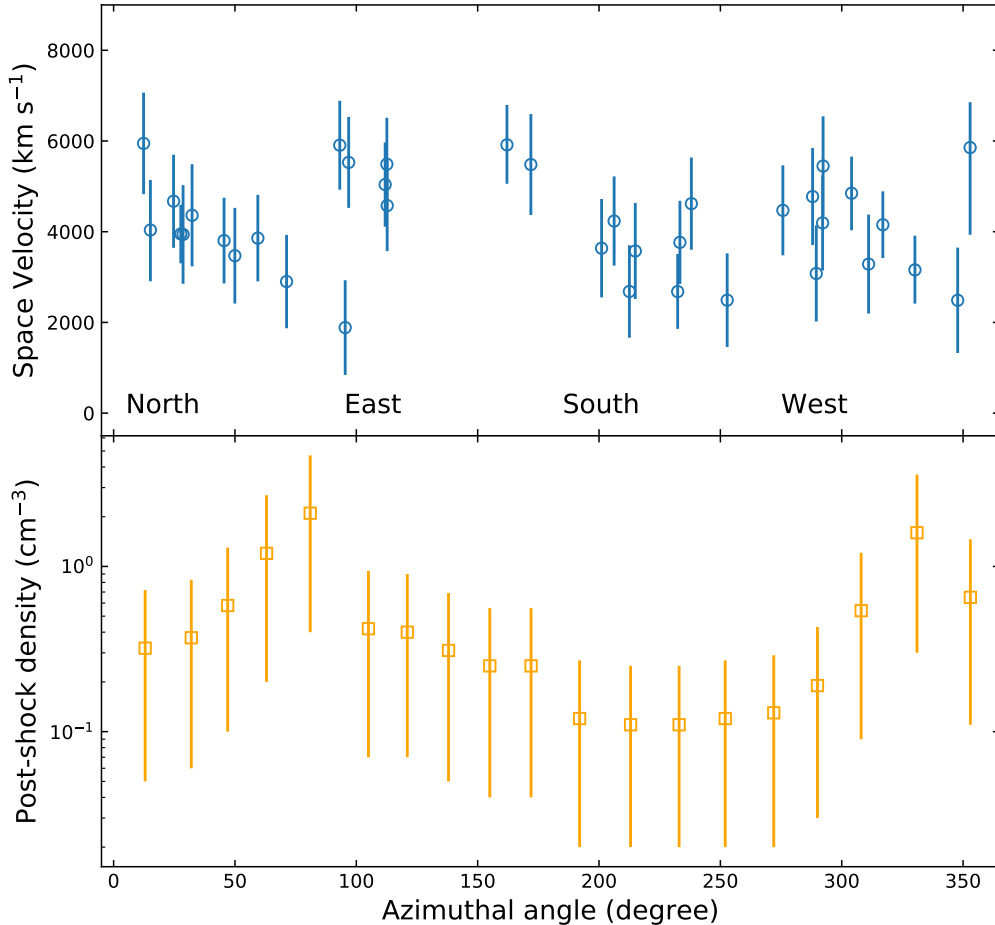


Figure 5. The upper panel shows the azimuthal distribution of our estimated ejecta space velocities in Tycho. The bottom panel shows the estimated post-shock densities along the rim from Williams et al. (2013).

present (Sato & Hughes 2017b; Millard et al. 2020). Our 3-D reconstruction of the ejecta distribution based on our radial velocity and proper motion measurements for a number of clumpy ejecta features indicates a relatively similar ejecta distribution between the eastern and western shells (Figures 6d). On the other hand, we find that the southern shell is dominated by redshifted ejecta (23 redshifted vs 6 blueshifted), while the majority of clumpy ejecta features in the northern shell are blueshifted (13 blueshifted vs 8 redshifted, see Figures 6b and 6c). The Chandra ACIS study by SH17a similarly revealed more blueshifted Si He-like and S He-like line-center energies in the north than in the south. The authors suggested that the observed discrepancy may be caused by a density enhancement of $\lesssim \sqrt{3}$ on the near side of the SNR compared with the far side. In this scenario, the density enhancement causes a stronger reverse shock on the northern near side. Thus, more reverse-shocked ejecta is observed in the north than in the south. A similar scenario could account for the north-south (N-S) differential in ejecta knots on the far side of the SNR. This N-S asymmetry of ejecta due to ambient density variation may be supported by the interacting density variations as reported by Williams et al. (2013) and Katsuda et al. (2010).

Although a variation in the ambient gas density surrounding Tycho is a plausible origin for the N-S ejecta differential, we may also consider that it could be due to an asymmetry in the early ejecta distribution immediately after the explosion. Seitzzahl et al. (2013) simulated a range of Type Ia explosion scenarios and found that delayed detonation

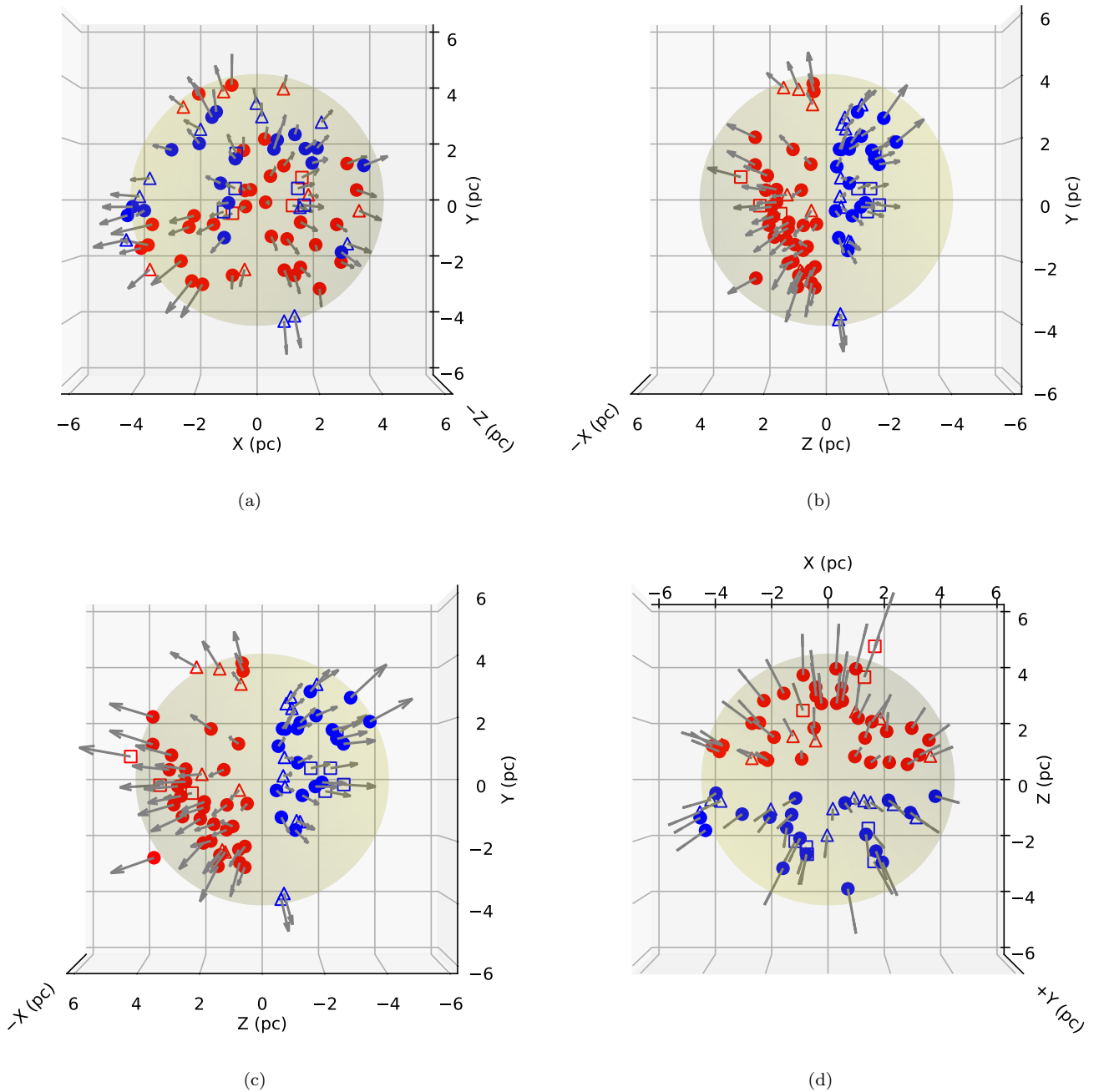


Figure 6. 3-D perspectives of the ejecta knots in Tycho. The red markers represent redshifted ejecta and blue are blueshifted ejecta. In (a) – (c), we also overlay the ACIS measurements of ejecta velocities by SH17a and W17. The circles, squares, and triangles show velocity measurements from our HETG sample, SH17a, and W17, respectively. For shared regions, we plot only our v_r values. For the ACIS data, we include only those high-velocity regions with $v_r > 900 \text{ km s}^{-1}$ (the ACIS systematic gain shift uncertainty). For knots where the proper motion was measured, the arrows point in the direction of the estimated 3D velocity. For the rest of the sample, the arrows point from the SNR center to the position of the knot. The length of the arrow represents the magnitude of the space velocity for each knot. The pale shaded circle shows the approximate location of the main X-ray shell of Tycho. The axis along the line of sight increases into the page. In (a), the X and Y components represent the current locations based on each knot’s R.A. and decl. In (b), the Z component of each knot is the measured v_r multiplied by the age of the remnant. The Z component in (b) is likely underestimated due to the deceleration of the knots. In (c), the Z component from (b) is divided by the maximum forward shock expansion index, $\eta = 0.65$ (Katsuda et al. 2010) to show a general approximation of the current physical positions of knots along the line of sight, accounting for their deceleration. In (d), we show a “top-down” view of Tycho with the ejecta in the same positions as in (c). The Y-axis increases out of the page.

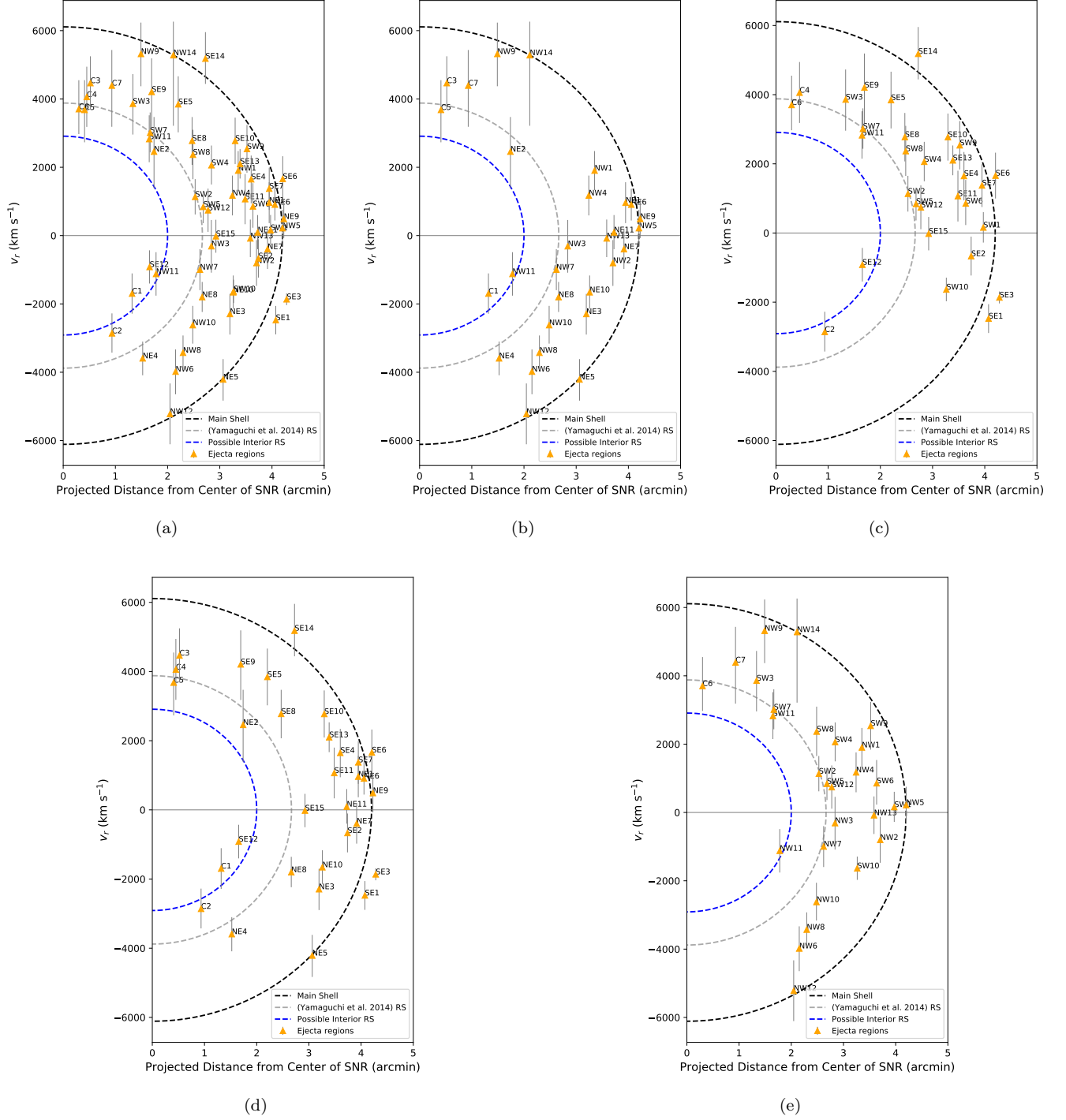


Figure 7. In panel (a), the positions of ejecta knots in v_r vs. r (projected angular distance from the center of the SNR) space. The black and gray dashed loci are the approximate locations of the outermost boundary of the main SNR shell and the reverse shock, respectively. The blue locus is a new potential reverse-shock location. A proportionality constant of $0''.041 \text{ (km s}^{-1}\text{)}^{-1}$ is applied to the loci based off the maximum expansion rate ($\sim 0.15 \text{ \% yr}^{-1}$) estimated by [Katsuda et al. \(2010\)](#). Panels (b), (c), (d), and (e) show those knots located only in the northern, southern, eastern, and western hemispheres, respectively.

(DDT) models with fewer ignition points resulted in more asymmetric explosions. [Ferrand et al. \(2019\)](#) propagated a fully 3D N100 DDT model of [Seitenzahl et al. \(2013\)](#) into the SNR stage. They found that asymmetries in the

explosion were required to explain the large-scale structures in X-ray maps of Tycho (specifically, the power spectrum of radius fluctuations around the rim, Warren et al. (2005)). Ferrand et al. (2021) further explored the early-stage evolutions of SNRs using the N5 (small number of ignition points) and N100 (large number of ignition points) DDT and pure deflagration models of Seitenzahl et al. (2013) and Fink et al. (2014). The authors found that the N5ddt models produce a more asymmetric, dipolar remnant whose imprint lasts up to a few hundred years. It is not straightforward to directly compare the results of these simulations with the non-uniform ejecta distribution inferred from our velocity measurements. However, our work suggests the presence of an aspherical ejecta velocity distribution in Tycho.

4.3. Explosion Center and Reverse Shock

We estimate the kinematic center of Tycho from our proper motion measurements of ejecta knots. We choose knots which have both $\mu_{R.A.}$ and $\mu_{decl.}$ greater than the systematic uncertainty. We generally follow the technique employed in Sato & Hughes (2017b). Initially, we assume that each knot has moved at its current proper motion speed since the explosion (i.e., $\eta = 1$) to estimate its 2-D starting position. We average the starting positions of all individual knots to calculate the tentative “initial” kinematic center. Then, we calculate the new expansion index for each knot based on this tentative kinematic center, and trace its motion back to a new starting point, this time dividing the distance traveled by the expansion index to account for its decelerated motion. We repeat this process until the average kinematic center converged on a single value (after about 25 iterations). Our estimated kinematic center is $R.A.(J2000) = 00^{\text{h}}25^{\text{m}}18^{\text{s}}.725 \pm 1^{\text{s}}.157$ and $decl.(J2000) = +64^{\circ}08'02''.5 \pm 11''.2$. This position is $\sim 13''$ southwest of the geometric center estimated by Warren et al. (2005). The previously suggested candidates for the companion of Tycho’s progenitor, Tycho G (Ruiz-Lapuente et al. 2004), Tycho E (Ihara et al. 2007), and Tycho B (Kerzendorf et al. 2013, 2018), are located approximately $33''$ E, $14''$ NE, and $17''$ NW from our estimated center, respectively. Assuming a distance of 3.5 kpc, their transverse velocities since the explosion would be $\sim 1200 \text{ km s}^{-1}$, 500 km s^{-1} , and 600 km s^{-1} , respectively. This is in contrast to their recently measured proper motions (Kerzendorf et al. 2013), which would imply transverse velocities of $100 - 200 \text{ km s}^{-1}$. However, since the positions of Tycho E and Tycho B are within a few arcseconds of the error ellipse of our estimated center (see Figure 4), they may have travelled a shorter distance if our kinematic center is representative of the explosion site. Thus, their transverse velocities since the explosion could be significantly slower, in line with the current values. Tycho G is located several arcseconds outside of the error ellipse, and therefore its current proper motion is still too low to account for the angular distance it would have travelled from our kinematic center since the explosion.

We plot our measured radial velocity for each knot against its angular distance from the center of the SNR in Figure 7a. Figures 7b and 7c show the north–south asymmetry discussed in Section 4.2, and Figures 7d and 7e show ejecta features projected in the eastern and western hemispheres, respectively. We plot the main shell (the forward shock) and the reverse shock position from Yamaguchi et al. (2014) estimated from the location of Fe $K\beta$ emission generally in the NW quadrant of Tycho. The bulk of the ejecta knots in our sample are positioned between the forward and reverse shocks, as expected. However, there are several knots positioned closer to the SNR center beyond the reverse shock. The locus of these inner ejecta knots appears to form a smaller reverse shock at $\sim 2.0'$ from the SNR center, or 75% of the $2.6'$ radius for the reverse shock estimated by Yamaguchi et al. (2014). According to models of dynamical evolution of SNRs (Truelove & McKee 1999) with an explosion energy of 1.2×10^{51} ergs (Badenes et al. 2006) and an ejected mass of $1.4 M_{\odot}$, ambient density variation by a factor of ~ 4 (similar to that reported by Williams et al. (2013) for Tycho) may produce $\sim 30\%$ deeper-reaching reverse shock. These knots beyond the reach of the previously-known reverse shock are blueshifted, and therefore are positioned on the near side of the SNR. Thus, these inner ejecta knots may represent deviated parts of the reverse shock due to the shock interaction with denser medium on the near side of the SNR. Recently, X-ray proper motion measurements of Tycho’s forward shock showed that its expansion has significantly decelerated from 2003 to 2015 (down to 40% of its initial value, Tanaka et al. (2021)). The authors suggested that the forward shock may be encountering a non-uniform wall of dense gas, possibly created from the winds of the progenitor system. Our results may support the presence of a similar density variation along the line of sight.

5. CONCLUSIONS

We have measured the radial velocities of 59 small ejecta features in Tycho’s SNR using our deep 450 ks Chandra HETG observation. Based on these measurements, our 3–D reconstruction of Tycho shows a large-scale asymmetry where most knots in the northern half are blueshifted and thus on the near side, and most knots in the southern half

are redshifted and therefore are located on the far side. Ambient density variations across the near and far sides of the remnant might have caused non-uniformity in the formation of reverse shock, and thus resulted in the differences in the frequency of detected ejecta knots. Alternatively, the identified asymmetry could be caused by a non-spherical explosion of the progenitor.

For 37 of the 59 ejecta features in our sample, we measured their proper motions using archival Chandra ACIS data. We estimate an expansion center based on our measured proper motions. Combining the radial velocities and proper motions, we find space velocities up to 6000 km s⁻¹. The azimuthal distribution of our measured space velocities shows generally higher speeds of ejecta towards the SE. Regions with low velocity coincide with higher ambient density at the rim. However, the high-velocity SE regions do not coincide with comparatively lower ambient densities, and therefore probably resulted from higher kinetic energy being deposited in that direction from the explosion. Based on our detection of relatively lower radial velocities for several ejecta knots projected near the center of the SNR, we postulate a considerable ambient density variation along the line of sight (e.g., a higher density on the near side of Tycho).

This work has been supported in part by NASA Chandra Grant GO7-18061X. TS was supported by the Japan Society for the Promotion of Science (JSPS) KAKENHI grant No. JP19K14749. JPH acknowledges support from NASA grant number NNX15AK71G to Rutgers University. We thank the anonymous referee for their useful recommendations that improved the explication of this work.

REFERENCES

- Arnaud, K. A. 1996, in *Astronomical Society of the Pacific Conference Series*, Vol. 101, *Astronomical Data Analysis Software and Systems V*, ed. G. H. Jacoby & J. Barnes, 17
- Badenes, C., Borkowski, K. J., Hughes, J. P., Hwang, U., & Bravo, E. 2006, *ApJ*, 645, 1373, doi: [10.1086/504399](https://doi.org/10.1086/504399)
- Borkowski, K. J., Lyerly, W. J., & Reynolds, S. P. 2001, *ApJ*, 548, 820, doi: [10.1086/319011](https://doi.org/10.1086/319011)
- Cash, W. 1979, *ApJ*, 228, 939, doi: [10.1086/156922](https://doi.org/10.1086/156922)
- Decourchelle, A., Sauvageot, J. L., Audard, M., et al. 2001, *A&A*, 365, L218, doi: [10.1051/0004-6361:20000115](https://doi.org/10.1051/0004-6361:20000115)
- Drake, G. W. 1988, *Canadian Journal of Physics*, 66, 586, doi: [10.1139/p88-100](https://doi.org/10.1139/p88-100)
- Fang, J., Yu, H., & Zhang, L. 2018, *MNRAS*, 474, 2544, doi: [10.1093/mnras/stx2921](https://doi.org/10.1093/mnras/stx2921)
- Ferrand, G., Warren, D. C., Ono, M., et al. 2019, *ApJ*, 877, 136, doi: [10.3847/1538-4357/ab1a3d](https://doi.org/10.3847/1538-4357/ab1a3d)
- . 2021, *ApJ*, 906, 93, doi: [10.3847/1538-4357/abc951](https://doi.org/10.3847/1538-4357/abc951)
- Fink, M., Kromer, M., Seitenzahl, I. R., et al. 2014, *MNRAS*, 438, 1762, doi: [10.1093/mnras/stt2315](https://doi.org/10.1093/mnras/stt2315)
- Foight, D. R., Güver, T., Özel, F., & Slane, P. O. 2016, *ApJ*, 826, 66, doi: [10.3847/0004-637X/826/1/66](https://doi.org/10.3847/0004-637X/826/1/66)
- Fruscione, A., McDowell, J. C., Allen, G. E., et al. 2006, in *Society of Photo-Optical Instrumentation Engineers (SPIE) Conference Series*, Vol. 6270, *Society of Photo-Optical Instrumentation Engineers (SPIE) Conference Series*, ed. D. R. Silva & R. E. Doxsey, 62701V, doi: [10.1117/12.671760](https://doi.org/10.1117/12.671760)
- Hayato, A., Yamaguchi, H., Tamagawa, T., et al. 2010, *ApJ*, 725, 894, doi: [10.1088/0004-637X/725/1/894](https://doi.org/10.1088/0004-637X/725/1/894)
- Houck, J. C., & Denicola, L. A. 2000, in *Astronomical Society of the Pacific Conference Series*, Vol. 216, *Astronomical Data Analysis Software and Systems IX*, ed. N. Manset, C. Veillet, & D. Crabtree, 591
- Huenemoerder, D. P., Mitschang, A., Dewey, D., et al. 2011, *AJ*, 141, 129, doi: [10.1088/0004-6256/141/4/129](https://doi.org/10.1088/0004-6256/141/4/129)
- Hwang, U., Hughes, J. P., & Petre, R. 1998, *ApJ*, 497, 833, doi: [10.1086/305501](https://doi.org/10.1086/305501)
- Ihara, Y., Ozaki, J., Doi, M., et al. 2007, *PASJ*, 59, 811, doi: [10.1093/pasj/59.4.811](https://doi.org/10.1093/pasj/59.4.811)
- Ishibashi, K., Dewey, D., Huenemoerder, D. P., & Testa, P. 2006, *ApJL*, 644, L117, doi: [10.1086/505702](https://doi.org/10.1086/505702)
- Jha, S., Kirshner, R. P., Challis, P., et al. 2006, *AJ*, 131, 527, doi: [10.1086/497989](https://doi.org/10.1086/497989)
- Katsuda, S., Petre, R., Hughes, J. P., et al. 2010, *ApJ*, 709, 1387, doi: [10.1088/0004-637X/709/2/1387](https://doi.org/10.1088/0004-637X/709/2/1387)
- Kerzendorf, W. E., Long, K. S., Winkler, P. F., & Do, T. 2018, *MNRAS*, 479, 5696, doi: [10.1093/mnras/sty1863](https://doi.org/10.1093/mnras/sty1863)
- Kerzendorf, W. E., Yong, D., Schmidt, B. P., et al. 2013, *ApJ*, 774, 99, doi: [10.1088/0004-637X/774/2/99](https://doi.org/10.1088/0004-637X/774/2/99)
- Krause, O., Birkmann, S. M., Usuda, T., et al. 2008a, *Science*, 320, 1195, doi: [10.1126/science.1155788](https://doi.org/10.1126/science.1155788)
- Krause, O., Tanaka, M., Usuda, T., et al. 2008b, *Nature*, 456, 617, doi: [10.1038/nature07608](https://doi.org/10.1038/nature07608)
- Maeda, K., Leloudas, G., Taubenberger, S., et al. 2011, *MNRAS*, 413, 3075, doi: [10.1111/j.1365-2966.2011.18381.x](https://doi.org/10.1111/j.1365-2966.2011.18381.x)

- Marshall, H. L., Dewey, D., & Ishibashi, K. 2004, in *Society of Photo-Optical Instrumentation Engineers (SPIE) Conference Series*, Vol. 5165, X-Ray and Gamma-Ray Instrumentation for Astronomy XIII, ed. K. A. Flanagan & O. H. W. Siegmund, 457–468, doi: [10.1117/12.508320](https://doi.org/10.1117/12.508320)
- Millard, M. J., Bhalerao, J., Park, S., et al. 2020, *ApJ*, 893, 98, doi: [10.3847/1538-4357/ab7db1](https://doi.org/10.3847/1538-4357/ab7db1)
- Ruiz-Lapuente, P., Comeron, F., Méndez, J., et al. 2004, *Nature*, 431, 1069, doi: [10.1038/nature03006](https://doi.org/10.1038/nature03006)
- Sato, T., Bravo, E., Badenes, C., et al. 2020, *ApJ*, 890, 104, doi: [10.3847/1538-4357/ab6aa2](https://doi.org/10.3847/1538-4357/ab6aa2)
- Sato, T., & Hughes, J. P. 2017a, *ApJ*, 840, 112, doi: [10.3847/1538-4357/aa6f60](https://doi.org/10.3847/1538-4357/aa6f60)
- . 2017b, *ApJ*, 845, 167, doi: [10.3847/1538-4357/aa8305](https://doi.org/10.3847/1538-4357/aa8305)
- Sato, T., Hughes, J. P., Williams, B. J., & Morii, M. 2019, *ApJ*, 879, 64, doi: [10.3847/1538-4357/ab24db](https://doi.org/10.3847/1538-4357/ab24db)
- Sato, T., Katsuda, S., Morii, M., et al. 2018, *ApJ*, 853, 46, doi: [10.3847/1538-4357/aaa021](https://doi.org/10.3847/1538-4357/aaa021)
- Seitzzahl, I. R., Ciaraldi-Schoolmann, F., Röpke, F. K., et al. 2013, *MNRAS*, 429, 1156, doi: [10.1093/mnras/sts402](https://doi.org/10.1093/mnras/sts402)
- Tanaka, T., Okuno, T., Uchida, H., et al. 2021, *ApJL*, 906, L3, doi: [10.3847/2041-8213/abd6cf](https://doi.org/10.3847/2041-8213/abd6cf)
- Truelove, J. K., & McKee, C. F. 1999, *ApJS*, 120, 299, doi: [10.1086/313176](https://doi.org/10.1086/313176)
- Vancura, O., Gorenstein, P., & Hughes, J. P. 1995, *ApJ*, 441, 680, doi: [10.1086/175391](https://doi.org/10.1086/175391)
- Wang, C.-Y., & Chevalier, R. A. 2001, *ApJ*, 549, 1119, doi: [10.1086/319439](https://doi.org/10.1086/319439)
- Wang, L., & Wheeler, J. C. 2008, *ARA&A*, 46, 433, doi: [10.1146/annurev.astro.46.060407.145139](https://doi.org/10.1146/annurev.astro.46.060407.145139)
- Warren, J. S., Hughes, J. P., Badenes, C., et al. 2005, *ApJ*, 634, 376, doi: [10.1086/496941](https://doi.org/10.1086/496941)
- Williams, B. J., Borkowski, K. J., Ghavamian, P., et al. 2013, *ApJ*, 770, 129, doi: [10.1088/0004-637X/770/2/129](https://doi.org/10.1088/0004-637X/770/2/129)
- Williams, B. J., Katsuda, S., Cumbee, R., et al. 2020, *ApJL*, 898, L51, doi: [10.3847/2041-8213/aba7c1](https://doi.org/10.3847/2041-8213/aba7c1)
- Williams, B. J., Coyle, N. M., Yamaguchi, H., et al. 2017, *ApJ*, 842, 28, doi: [10.3847/1538-4357/aa7384](https://doi.org/10.3847/1538-4357/aa7384)
- Wilms, J., Allen, A., & McCray, R. 2000, *ApJ*, 542, 914, doi: [10.1086/317016](https://doi.org/10.1086/317016)
- Yamaguchi, H., Hughes, J. P., Badenes, C., et al. 2017, *ApJ*, 834, 124, doi: [10.3847/1538-4357/834/2/124](https://doi.org/10.3847/1538-4357/834/2/124)
- Yamaguchi, H., Eriksen, K. A., Badenes, C., et al. 2014, *ApJ*, 780, 136, doi: [10.1088/0004-637X/780/2/136](https://doi.org/10.1088/0004-637X/780/2/136)